Optics Letters

Spatial–temporal phase demodulation decoding superimposed ghost reflections in optical testing

Sotero Ordones,[1] Jae-Hyeung Park,[2] Henry Quach,[1] Daewook Kim,[1,3,4] and Heejoo Choi[1,3,*]

[1]Large Optics Fabrication and Testing Group, Wyant College of Optical Sciences, University of Arizona, 1630 E. University Blvd., Tucson, Arizona 85721, USA
[2]Department of Information and Communication Engineering, Inha University, Incheon, 22212, Republic of Korea
[3]Large Binocular Telescope Observatory, University of Arizona, Tucson, Arizona 85721, USA
[4]Department of Astronomy and Steward Observatory, University of Arizona, 933 N. Cherry Ave., Tucson, Arizona 85721, USA
*Corresponding author: heejoochoi@email.arizona.edu

Received 16 June 2022; revised 9 July 2022; accepted 15 July 2022; posted 19 July 2022; published 8 August 2022

We introduce a method of phase demodulation to distinguish the ghost reflection commonly observed in optical testing. The method digitally processes a sequence of fringe patterns to separate the reflections from the front and rear surfaces. First, we use a phase-shifting algorithm to compute an analytic signal with the two reflections coupled, and then we decouple them through a maximized spatial filtering. The process requires the acquisition of at least three fringe patterns, as well as fulfilling opposite signs for the magnifications of the two reflections. We demonstrate the decoding process through a real phase measuring deflectometry data processing example.

https://doi.org/10.1364/OL.468063

Introduction. It is well-known that sinusoidal patterns are ubiquitous due to their mathematical efficiency in information retrieval and their natural emergence in interferograms. Regardless of the data acquisition method, sinusoidal patterns have the intrinsic properties of phase and amplitude which are visually distinct and mathematically retrievable after a single reflection. However, transparent media such as refractive optics invoke Fresnel reflection at both the front and rear surfaces. The rear ghost reflection superimposes itself upon the image formed by the frontal surface. This ghost reflection easily breaks the information in the phase retrieving process, and the calculated phase loses its fidelity.

Phase measuring deflectometry (PMD) has been used widely due to its flexibility and accuracy. Deflectometry is a non-null testing that provide interferometric-level accuracy surface maps from traditional optics testing to freeform optics, depending on the quality of calibration [1]. However, the testing of refractive surfaces also suffers from ghost reflection, as shown in Fig. 1. The reflected fringe images from the frontal testing surface and rear surface are superimposed at the imaging detector, which erodes the original phase information.

In the literature, there has been some work toward reconciling this ghost reflection. The double reflection issue has been addressed algorithmically by employing multiple frequency patterns. Huang and Asundi [2] have proposed a two-step method to deal with the double reflection by utilizing an extra pair of sheared frequency fringe patterns. First, the authors employ a four-step phase-shifting algorithm to retrieve those analytic signals, having coupled the phase from the two surfaces. Then, they obtained both unwrapped phase maps through a nonlinear regression for each pixel. Although the Levenberg–Marquardt iteration can decouple both signals effectively, it requires not only a well-selected starting of phase retrieving approximation but also a suitable demodulation path. In this sense, Leung and Cai [3] depict not only the complexity and importance of choosing a good starting point but also that this method can fail in some pixels.

Wang and collaborators [4] have proposed to remove the second reflection by using frequency-domain filtering on the temporal spectrum. The authors acquired 1000 frequency-shifted fringe images to thoroughly sample the temporal fringe's spectrum, hence, they can carry out the frequency-domain filtering in a pixelwise manner. Whence the phase retrieval can meet high accuracy since the filtering is pixelwise. Nonetheless, this approach requires thousands of images for accurate phase retrieval, which can be impractical. Moreover, the authors must adjust the filter's frequency response for each pixel since the temporal spectrum depends mainly on the phase values at each pixel.

Siwei and colleagues [5] proposed their envelope curve algorithm, which consists of hybrid least squares fitting the temporal, multi-frequency fringe in a pixel-by-pixel manner. This algorithm first carries out a linear regression to estimate the linear variables, and then these estimates are utilized to retrieve the nonlinear variables through nonlinear least squares regression. The authors perform these two regressions iteratively until it meets the convergence criterion. This iterative algorithm needs a well-selected starting approximation to meet the suitable optimum for the nonlinear variables and 500 fringe images. We noted that this algorithm is significantly slow and computationally expensive because of both the long acquisition time and the use of nonlinear regression.

Recently, Ye *et al.* [6] have proposed a purely linear, iterative algorithm to decouple both signals of the front and rear surfaces. The authors obtain an equivalent over-determined linear system

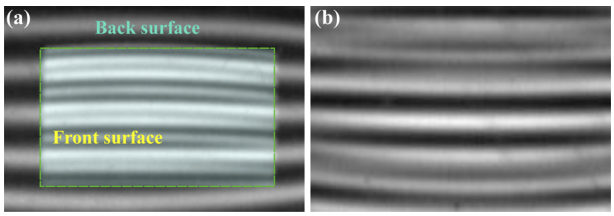

Fig. 1. Acquired deflectograms showing front and back surface reflection where we observe the ghost image during PMD testing: (a) plano–convex lens [67.7 mm radius of curvature (RoC)] and (b) plano–concave (−66.0 mm RoC).

of equations. However, the coefficient matrix and response variable depend on one another, translating into the linear system is numerically unstable. Thence, one must provide a finely selected starting point to get a suitable solution, or else it may diverge. Furthermore, the numerical instability is more severe as the phase differences become tiny. For the case that the front and rear surfaces are significantly different from one another and a good starting point is selected, this algorithm would retrieve both surfaces well, while requiring around 30 images to retrieve the surfaces.

We note that the correct selection of the starting points for regressive methods requires prior information about the testing. It is well-known that starting points are crucial for nonlinear optimization and solving numerically unstable problems. In this Letter, we introduce a novel temporal–spatial method for phase demodulation of deflectograms in the presence of ghost reflection. Our method needs at least three fringe images and does not require prior information about the testing surfaces. Our proposal consists of firstly computing the analytic signal through a phase-shifting algorithm (PSA), and then both phases are decoupled by frequency-domain filtering of the analytic signal retrieved by the PSA.

Theoretical framework. One particularly useful benefit of deflectometry is the flexibility of the system layout. When the unit under test (UUT) is the lens, we can adjust the distance between the lens and monitor to have the layout shown in Fig. 2. In this configuration, image magnification from the front and back surfaces has an inverted sign. The monitor images are flipped in the camera view through the front and back surfaces. The phase shift along the monitor is implemented in the general operation of the phase measuring deflectometry. So, in the configuration in Fig. 2(a), the front and back surface images have opposite phase flow directions. The proposed approach leverages this flipped sign in the phase domain, as shown in Eq. (2) the + and − sign in front of y. Considering that fringes are horizontally oriented, the intensity distribution of the temporal sequence of superimposed patterns can be described by

$$I(r,t) = a(r) + b_1(r)\cos\left[\varphi_1(r) + \omega_0 t\right] + b_2(r)\cos\left[\varphi_2(r) + \omega_0 t\right], \tag{1}$$

where $r = r(x,y)$ is the pixel position; ω_0 denotes the temporal phase carrier; the background intensity is indicated by $a(r)$; $b_1(r)$ and $b_2(r)$ are the fringe modulation functions from the front and back surfaces, respectively; $\varphi_1(r)$ and $\varphi_2(r)$ mean, respectively, the searched phases from the front, $h_1(r)$, and back, $h_2(r)$, surfaces. These phase functions can be described as

$$\varphi_1(r) \propto v_1\left[\frac{\partial h_1(r)}{\partial y} + y\right], \tag{2a}$$

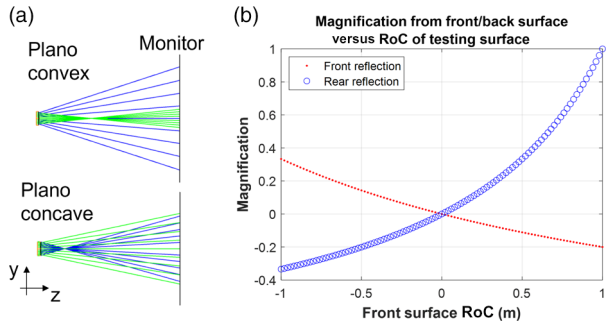

Fig. 2. Raytrace of plano–convex and plano–concave cases and their magnification. (a) Blue and green rays are reflected off the front and back surface, respectively. In the plano–convex case, the rays from the back surface are converged, and the flipped monitor images are relayed to camera. (b) Front and back surface magnification is always opposite in first-order optics. We admit that to leverage the inverse phase flow, a particular layout (e.g., the distance between UUT and monitor) is required.

$$\varphi_2(r) \propto v_2\left[\frac{\partial h_2(r)}{\partial y} - y\right], \tag{2b}$$

where $v_1 = 2\pi/T_1$ is the fringe frequency observed in the front surface being T_1 its fringe period on the screen; $v_2 = 2\pi/T_2$ comes from the back surface. As mentioned prior, the phase flow of the front and back surfaces are opposite each other, so the flipped sign (or *vice versa*) in Eq. (1) is always correct. We notice that the opposite sign of the phase flow is vital for our technique that we are describing.

We now analyze the spectral characteristics of the intensity distribution in Eq. (1). By taking the temporal Fourier transform of $I(t)$, we obtain the temporal spectrum as

$$\begin{aligned} I(\omega) = \mathcal{F}_t\{I(t)\} = a\delta(\omega) &+ \frac{1}{2}\left[b_1 e^{i\varphi_1} + b_2 e^{i\varphi_2}\right]\delta(\omega-\omega_0) \\ &+ \frac{1}{2}\left[b_1 e^{-i\varphi_1} + b_2 e^{-i\varphi_2}\right]\delta(\omega+\omega_0), \end{aligned} \tag{3}$$

at pixel r; where $\mathcal{F}_t\{\cdot\}$ is the operator of the temporal Fourier transform, and $\delta(\cdot)$ is Dirac's delta function. From Eq. (3), we can realize that this temporal spectrum has three spectral components, particularly, the searched component at $\omega = \omega_0$ contains the sum of the two searched signals; see Fig. 3(a). Thence, the searched signals cannot be decoupled by means of a PSA since front and back signals are located at the same frequency ω_0. We want to point out that this fact is not due to the number of equations and unknown variables as many previous publications have mentioned, but rather this is because PSAs are linear approaches and this problem is ill-conditioned for the temporal domain. Refer to Ref. [7] for a spectral and algebraic analysis of PSAs.

On the other hand, the spatial spectrum of $I(r)$ is given by

$$\begin{aligned} I(q) = \mathcal{F}_r\{I(r)\} = A(q) &+ \frac{e^{i\omega_0 t}}{2}\left[C(q-q_1) + D(q-q_2)\right] \\ &+ \frac{e^{-i\omega_0 t}}{2}\left[C^*(-q-q_1) + D^*(-q-q_2)\right], \end{aligned} \tag{4}$$

at certain moment t. Here $\mathcal{F}_r\{\cdot\}$ is the operator of the spatial Fourier transform; superscript * indicates complex conjugation; $q = q(u,v)$ is the radial-frequency position. Here $A(q)$ is the spectrum of the intensity background (DC term); $C(q-q_1) =$

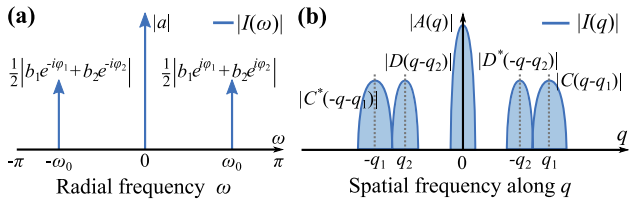

Fig. 3. Schematic description of the spectra of the superimposed fringe patterns: (a) temporal and (b) spatial. It is noticeable the spectrum overlapping between the lobe $C(q-q_1)$ and $D^*(-q-q_2)$, and also between $C^*(-q-q_1)$ and $D(q-q_1)$.

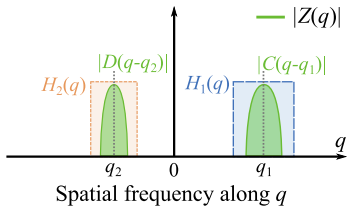

Fig. 4. Schematic description of the analytic signal's spectrum computed by the PSA. Note that this spectrum has two well-separated components which could be decoupled using two spatial filters $H_1(q)$ and $H_2(q)$ as illustrated.

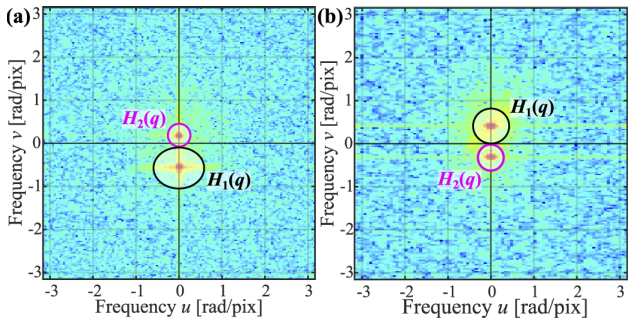

Fig. 5. Frequency-domain filtering of the analytic signal estimated by the PSA: (a) plano–convex data and (b) plano–concave data. Note that the filters $H_1(q)$ and $H_2(q)$ may not be the same for both spectral components.

$\mathcal{F}_r\{b_1(r)\exp[i\varphi_1(r)]\}$ is the searched signal of the front surface being $q_1 \leftarrow v_1$ the observed phase carrier; $D(q-q_2) = \mathcal{F}_r\{b_2(r)\exp[i\varphi_2(r)]\}$ corresponds to the searched signal of the back surface being its $q_2 \leftarrow -v_2$ the spatial phase carrier. Assuming that $v_1 > v_2$, then the spatial spectrum can be depicted by Fig. 3(b), from which one can see the correct sign of the phase is on the right-hand side for the front surface, $C(q-q_1)$, whereas on the left-hand side for the back surface, $D(q-q_2)$. The spatial spectrum will have this behavior provided that the conditions in Eq. (2) are fulfilled. Furthermore, we can straightforwardly realize that one searched signal will be on the left-hand side of the spatial spectrum and the other on the right-hand side as long as only one fringe pattern (of the two) is imaging inversely (negative magnification), i.e., $\pm v_1$ while $\mp v_2$.

Based on the previous characteristics of both temporal and spatial spectra, we propose to retrieve the two phase maps using a temporal–spatial approach. Our proposal consists of first computing an initial analytic signal using a PSA, and then spatially decoupling the two phase maps through a frequency-domain spatial filtering. Based on the frequency transfer function (FTF) formalism for PSA [7], we first compute temporally the initial analytic signal as

$$z = \frac{1}{2}\left[b_1 e^{i\varphi_1} + b_2 e^{i\varphi_2}\right] = I(t) * h(t)\big|_{t=N-1} = \sum_{n=0}^{N-1} c_n^* I_n, \qquad (5)$$

for all pixels r. Here $I_n = I(t_n)$ is the nth superimposed fringe pattern, and $h(t)$ indicates the PSA's impulsive response with coefficients $c_n^* = (1/N)\exp(-in\omega_0)$, or the complex conjugate of c_n. These coefficients come from Bruning's formula and correspond to the least squares PSA [8]. Its FTF $H(\omega)$ accomplishes the quadrature conditions $H(0) = H(-\omega_0) = 0$ [7], and therefore retains only the right-sided Dirac delta function corresponding to $C + D$; see Fig. 3 and Eqs. (3) and (4). We do point out that we have been using only one PSA to retrieve the coupled analytic signal in Eq. (5), so the reader can realize that there is not a special PSA for front or back surfaces. Then, by taking the spatial Fourier transform of $z(r)$, we obtain the spectrum given by

$$Z(q) = \mathcal{F}_r\{z(r)\} = \frac{1}{2}C(q-q_1) + \frac{1}{2}D(q-q_2). \qquad (6)$$

Here, we can observe that the PSA allowed us to isolate the searched signals with the additional benefit that they are spectrally separated as sketched in Fig. 4. Since these spectral components are well-separated, we can decouple them utilizing frequency-domain filters. Let $H_1(q)$ and $H_2(q)$ be the spatial frequency responses of two filters being tuned at q_1 and q_2, respectively. Then, we can retrieve the final analytic signals by frequency-domain spatial filtering as

$$\frac{b_1(r)}{2}e^{i\varphi_1(r)} = \mathcal{F}_r^{-1}\{Z(q)H_1(q)\}, \qquad (7)$$

$$\frac{b_2(r)}{2}e^{i\varphi_2(r)} = \mathcal{F}_r^{-1}\{Z(q)H_2(q)\}. \qquad (8)$$

Since the conditions in Eq. (2) govern the disposition of the spectrum on Eq. (6), we notice that the distance $v_1 + v_2$, between the two spectral components, can allow the employing of broadband filters with the aim of getting enough amounts of spectral information, which it is not allowed via traditional frequency domain filtering. To this end, one should increase the filter's bandwidth through optimizing this distance by means of decreasing the pitch of the projected fringes. We simulated the challenging ghost reflection cases and the proposed method show 0.028 % error in retrieved phase map (see Supplement 1 for simulation result).

Experimental results. We now draw the effectiveness of our approach for phase retrieval with the experimental data from Fig. 1. Figure 5 illustrates the frequency-domain filtering of the two analytic signals coming from the plano–convex [Fig. 5(a)] and plano–concave [Fig. 5(b)]. The frequency of the plano–concave case is a very challenging case for general frequency domain filtering because the frequencies of the front and back surfaces are similar to each other and both spectra are overlapped. This will also occur when the RoC of the UUT is small as shown in Fig. 2. The proposed filtering could clean up redundant spectral information even though they are mostly overlapped. In the same vein, the spectral width of the determining filter is large enough to keep sufficient spectral information translating to an accurate phase estimation.

Fig. 6. Plano–concave experimental data: (a) superimposed pattern exhibiting ghost reflection; and the fringe patterns from the decoupled surfaces (b) concave (top) and (c) plano (bottom).

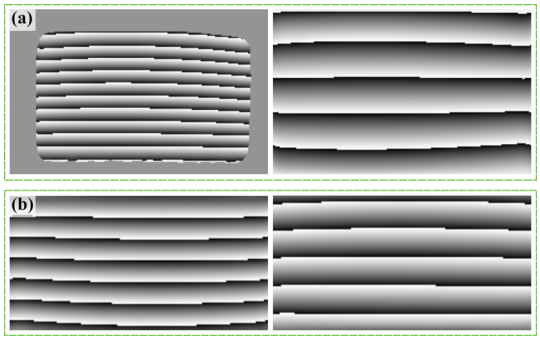

Fig. 7. Calculated wrapped phase maps from the series of phase shifting images from (a) plano–convex lens (b) plano–concave lens. Left and right subpanels are front and back surface phase, respectively. Note that we use the different size field of view (FoV).

Figure 6 depicts the results of the extracted fringes images of the plano–concave case. The amplitude is fully recovered without any distortion and fringe-print-through. In the PMD data process, the phase is calculated from the intensity variation of the individual pixel while the phase shifts. The fluctuation of the amplitude can be a serious phase error source but this error did not occur since the frequency filtering does not lose essential information. The series of the phase shifting images are processed, and decoupled fringe maps are used for phase calculation.

In Fig. 7, the calculated wrapped phases maps are shown. As aforementioned, we adjusted the deflectometry layout to have the inverted phase flow direction of front and back surfaces. In the case of the plano–convex [Fig. 7(a)], the phase direction is bottom-up in the front phase (left) and it reverses in the back surface phase (right).

When the retrieved phase (Fig. 7) has the fractured phase (e.g., ghost reflection and fringe-print-through), the unwrapped phase shows the distinct discontinuity due to the broken phase information. The unwrapping process is implemented on Fig. 8 via employing the algorithm in Ref. [9]. In Fig. 8, the *y*-profile confirmed the continuity of the unwrapped map.

We notice that although the experimental verification is presented for plano–convex and plano–concave cases, the proposed method can be applied to other cases as long as Eq. (2) is satisfied. Furthermore, the proposed method can be also utilized in interferometry or other optical metrology techniques provided that the Eq. (2) is satisfied.

Conclusion. We introduced a novel technique that can cope with optical metrology's double reflection issue using a two-step phase retrieval approach. Firstly, it consists of getting two coupled analytic signals through a phase-shifting algorithm and then decoupling them through frequency-domain spatial filtering of the analytic signals. Finally, we obtain the clear

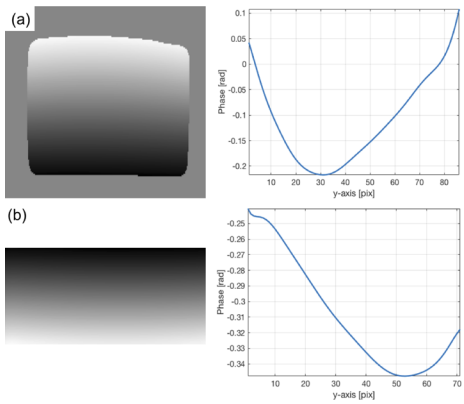

Fig. 8. Unwrapped phase maps and profile plot along the *y* axis: (a) plano–convex lens and (b) plano–concave lens. The center of the surface in Fig. 7 are cropped out and Zernike removal is applied for profile plot.

separated fringe images from the decoupled analytic signals without cross talking. The processed fringes images are further processed via phase unwrapping calculations and the validity is checked via continuity of phase map profile. This method shows perfect separation even in the case of the fully overlapped frequency from ghost reflection in the frequency domain. Since the unwanted frequency information is placed at the opposite quadrant of the frequency domain, a reasonably large filter could be adopted, enabling it to include sufficient frequency information. It minimizes information loss and increases the accuracy of decoupling. We admit that a specific deflectometry system layout is required to have the inverted phase flow from the front and back surfaces. However, PMD can easily adjust the optical layout compared with the other optical testing methods such as phase-shifting interferometry. This concept can be extended to suppressing even rear surface ghosts in plane-parallel plates (PPP). By placing the flat face of an auxiliary plano–convex optic against the PPP and index-matching their gap, the inverted sign magnification requirement is met.

Disclosures. The authors declare no conflicts of interest.

Data availability. Data underlying the results presented in this Letter are not publicly available at this time but may be obtained from the authors upon reasonable request.

Supplemental document. See Supplement 1 for supporting content.

REFERENCES

1. P. Su, R. E. Parks, L. Wang, R. P. Angel, and J. H. Burge, Appl. Opt. **49**, 4404 (2010).
2. L. Huang and A. K. Asundi, Meas. Sci. Technol. **23**, 085201 (2012).
3. Y.-C. Leung and L. Cai, Appl. Opt. **61**, 208 (2022).
4. R. Wang, D. Li, L. Li, K. Xu, L. Tang, P. Chen, and Q. Wang, Opt. Eng. **57**, 1 (2018).
5. T. Siwei, Y. Huimin, C. Hongli, W. Tianhe, C. Jiawei, W. Yuxiang, and L. Yong, Results Phys. **15**, 102734 (2019).
6. J. Ye, Z. Niu, X. Zhang, W. Wang, and M. Xu, Opt. Lasers Eng. **137**, 106356 (2021).
7. S. Ordones, M. Servin, M. Padilla, A. Mu noz, J. L. Flores, and I. Choque, Opt. Lett. **44**, 2358 (2019).
8. J. H. Bruning, D. R. Herriott, J. E. Gallagher, D. P. Rosenfeld, A. D. White, and D. J. Brangaccio, Appl. Opt. **13**, 2693 (1974).
9. A. Asundi and Z. Wensen, Appl. Opt. **37**, 5416 (1998).